Impact of shell-opening of a model razor clam on the evolution of force chains in granular media

Huang, S., S.M.[1], Mahabadi, N., A.M.[2], and Tao, J., A.M.[3]

[1]PhD Student, Center for Bio-mediated and Bio-inspired Geotechnics (CBBG), Arizona State University, Tempe, AZ. Email: shuang64@asu.edu

[2]Assistant Research Professor, Center for Bio-mediated and Bio-inspired Geotechnics (CBBG), Arizona State University, Tempe, AZ. Email: nariman.mahabadi@asu.edu

[3]Associate Professor, Center for Bio-mediated and Bio-inspired Geotechnics (CBBG), Arizona State University, Tempe, AZ. Email: julian.tao@asu.edu

ABSTRACT

The razor clams alternately inflate the shelled body and the muscular foot when burrowing down to the ground. It is found from previous numerical simulations that inflation of the shelled body not only forms a firm anchor for the foot penetration, but also reduces penetration resistance; on the other hand, further foot penetration relaxes the shell anchorage, which may compromise the burrowing effectiveness and efficiency. This study utilizes a photoelasticity-based technology, augmented with image processing, to validate the numerical findings. A simplified penetrator model composed of an expandable rectangular shell and a protrusible triangular foot is designed and incorporated into a transparent cell containing more than four thousand photoelastic disks. Sequential images are then taken during the model penetration, which include an initial foot penetration, followed by shell expansion and then another foot penetration. An image processing algorithm is developed to detect the evolution of grain contact forces (orientation and magnitude of contact forces) during the shell expansion and foot penetration of the model. Results from this study confirm the existence of the mutual influence between shell expansion pressure and foot penetration resistance: that is, increasing one causes reduction of the other and vice versa.

Keywords: force chains, photoelasticity, image processing, razor clam, penetration

INTRODUCTION

Soils are essentially assemblies of mineral particles, with air and water filling in the void spaces. Overlaid under gravitational effect, the soil becomes increasingly hard to be failed with depth (Budhu 2008; Das 2013) due to the increasing effective stress. Therefore, it is increasingly difficult to create space for common engineering activities as it goes deeper, such as sampling, pile installation, tunneling etc. Similarly, many burrowing organisms in nature locomote underground and encounter increasing resistance with depth. Nevertheless, by adopting various strategies, they

can burrow at a depth effectively and efficiently. Typical examples include the sand swimmer, sandfish lizard, wiggling its body to move through the sands (Maladen et al. 2011); the earthworms cyclically cracking the soil ahead to locomote through their substrate (Dorgan 2015); also, the plant roots penetrating into the soil by alternating growing in radial and longitudinal direction (Abdalla et al. 1969).

The Atlantic razor clam (*Ensis directus*) has been attractive to engineers because of its exceptional underground burrowing ability through a simple body structure and control strategy (Huang and Tao 2018a; Jung et al. 2011). The body structure of the razor clam is composed of a rigid shell and a hollow muscular foot, which serve as two alternate anchor points for the burrowing. During the burrowing process, the shell opens and forms a penetration anchor by compressing the surrounding soil; with this penetration anchor, the foot extends downward in a pulse-like manner until reaching the maximum foot extension; afterwards, the shell then closes, pushing body liquid into and dilating the pedal (distal portion of the foot) to form the terminal anchor; with this terminal anchor, the razor clam drags the shell downward and the whole body returns to the initial shape, as presented in Figure 1. These four consecutive steps constitute a typical burrowing cycle; the entire burrowing process is essentially an accumulation of multiple burrowing cycles. Using the dual-anchor strategy, the razor clam obtains the thrust and anchorage to propel itself into the substrate. Such a simple control strategy and body structure inspire engineers in developing the next generation of subsurface autonomous robotic penetrator for a wide spectrum of applications, such as underground wireless sensing network, autonomous underground exploration, and contamination monitoring etc.

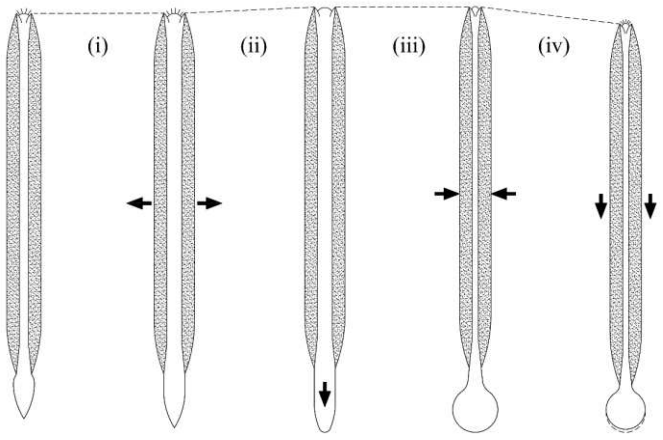

Figure 1. A typical burrowing cycle of the razor clam. The dotted line denotes the depth and arrows indicate the direction of movement of the foot and valves. (i) Opening of the valves. (ii) The foot probes downward. (iii) Valve adduction pushes body fluids into the foot to form a terminal anchor. (iv) The foot retracts, pulling the valves downward, and the body returns to its initial shape.

Previous works (Holland and Dean 1977; Trueman 1967) indicate that the average burrowing velocity of a razor clam can reach 1 cm/s, and that the submergence can be up to 70 cm (Holland and Dean 1977). However, the muscle strength of the razor clam only allows a body drag

up to 10 N (Trueman 1967), which can merely allow to push a razor-clam-shape aluminum rod into their substrate for 1 or 2 cm (Winter et al. 2012). (Winter et al. 2012) attributed the burrowing drag reduction and high energy efficiency to the 'localized fluidization' around the clam, which was caused by the closing and uplifting of the shelled body. And a robotic clam model (RoboClam) was designed to demonstrate the effect of fluidization (Winter et al. 2014). However, the roles of other steps (shell opening, foot extension and shell retraction) were not sufficiently addressed. Basically, the burrowing process contains complex soil-clam interactions. Interplay between any two neighboring steps exists and the contribution of each step to the locomotive effectiveness and efficiency may vary due to dynamic and cyclic nature of burrowing. Also, it is challenging to penetrate unsaturated soil or cohesive soil simply relying on localized fluidization. In the authors' previous work (Huang and Tao 2018b), penetration of a simplified clam-inspired penetrator in dry sands was modeled using Discrete Element Method. Results showed that the shell opening not only contributes to the formation of a penetration anchor, but also releases the stress in the soil around and below the foot, which causes resistance reduction during foot penetration; however, the subsequent foot penetration tends to weaken the penetration anchorage by reducing the normal confinement (or lateral earth pressure) applied on the expanded shell.

In this paper, a combined technique of photoelasticity and image processing is utilized to visualize the interplays among the shell-opening, foot penetration and the surrounding granular material. Findings from this study provide us an intuitive view on the soil-clam interactions and a sound reference for the future design of a self-burrowing robot.

METHODOLOGY

Experimental setup. Soils are opaque particulate materials. It is extremely challenging to see through the soil and observe the interactions among particles, or between particle and a structure, without using special techniques. The photoelasticity-based technology populates in visualizing the stress distribution and force chain network across a granular sample (Daniels et al. 2017). It relies on the polarization of light and the local-stress-dependent birefringence of the photoelastic material. When a photoleastic material is loaded, optical interference would occur in response to change of the local stress state and local refractive index of the material; as a result, a set of fringe pattern across the material will appear with the help of two polarizer filters which sandwich the material. The force chains within a photoelastic granular sample can then be visualized and quantified by analyzing the fringe patterns across the sample.

In this study, an experimental setup is designed to visualize the force chain evolution corresponding to the designed penetrator kinematics, as shown in Figure 2a. The penetrator is a simplified model to simulate the shell-foot structure of razor clams; it is composed of an expandable rectangular "shell" and a protrusible triangular "foot", as shown in Figure 2b. The expandable "shell" is composed of two major parts: a hollow rod with a wedge-like end (blue), sandwiched by two slender blocks (yellow) with an inner slope parallel to the wedge face; and a triangular foot (red), which is connected to a thin rod passing through the hollow rod. Three linear

actuators are utilized to control the shell expansion and foot penetration: by pulling the hollow rod upward using the two side-actuators, the wedge-like end enforces the two side-blocks to move laterally and therefore expands the "shell"; the central actuator then pushes the central thin rod downward and causes the triangular "foot" to penetrate. The fixation part (purple) above the "shell" is designed to limit the movement of the two side blocks in the horizonal direction, and to fix the entire penetrator at a desired location. The penetrator is incorporated into a transparent cell which contains more than four thousand photoelastic disks. A load cell is attached to the penetrator to monitor the resistive force during the test. The actuators and load cell are controlled using a microcontroller (Arduino Uno). The transparent cell is placed between two polarizer filters with a LED source at the back, and a camera is used to capture the real time image of the granular sample during the test.

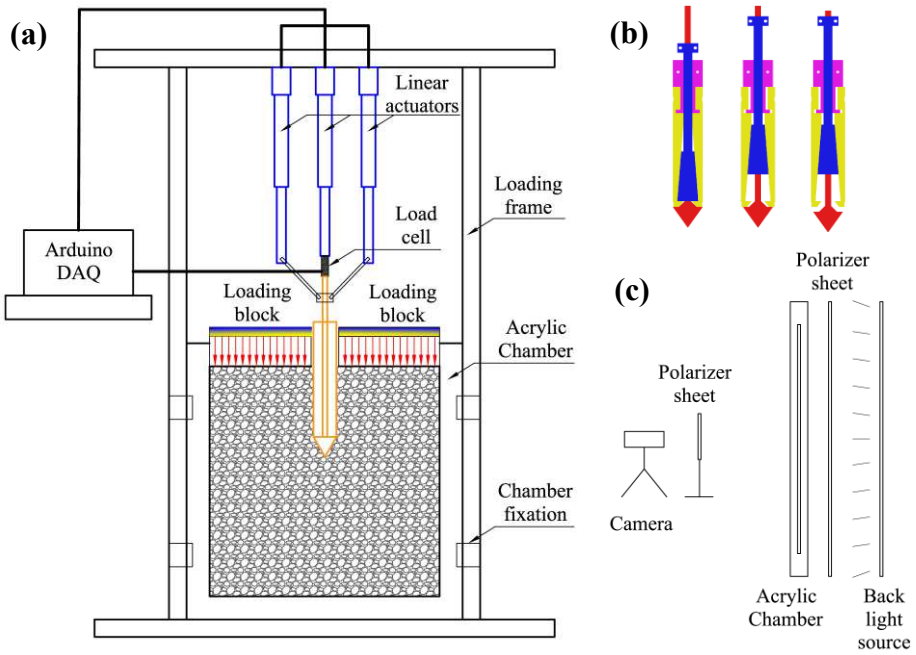

Figure 2. Experimental setup for the test. (a) the experiment scheme (b) the synthesized penetrator (c) side view showing the setup for camera and polarizer filters.

The designed penetrator is 5 cm in width with a 13.5 cm submergence into the granular sample. The sample size is 50 cm wide and 48 cm high, with the bottom and side boundaries fixed. A constant uniform vertical confinement of 200 N/m is applied at the top boundary with loading blocks. The ratio of penetrator width to the sample size is 10, so boundary effects are expected (Arroyo et al. 2011; Bolton et al. 1999). The system is actuated in order to achieve three sequential movements: penetrating the "foot" for 0.7 seconds (7 mm downward movement), expanding the "shell" for 2 seconds (3 mm lateral movement for each side) and penetrating the "foot" again for 1 second (10 mm downward movement). After each movement, the actuators are temporally paused for 8 seconds for image acquisition; in addition, images are taken in the middle of the

"shell" expansion process. A polarized and a non-polarized image are taken for each time with and without the filter, respectively.

Image processing. To quantify the force chain evolution, the image processing algorithm developed by Mahabadi and Jang (2017) was implemented. In general, a complete contact pair includes: size and position of the two contacting particles, and orientation and magnitude of the contact force. The non-polarized image is used to extract the particle positions and to detect the particle contacts; the corresponding polarized image is used to calculate the contact force magnitudes. Each image is a collection of pixels, and each pixel is a combination of three different colors (Red, Green, and Blue) with specific intensities ranging from 0 to 255. That is to say, each image can be treated as a combination of three different color matrices. To extract the particle information (including size and position), the non-polarized image is converted to a binary image based on the values of the red matrix of the image. An extended HoShen-Kopelman algorithm is then implemented to cluster and label all the identified particles. Hereafter, the pixel distances between any two neighboring pixels in the same particle are computed. The particle diameter is then determined as the longest distance, and the center of the identified diameter gives the center of the particle.

Once the size and position of all particles are extracted, the contacts among all the particles are detected by comparing the center distance between any two neighboring particles to the summation of their radii. If the summation of their radii is larger than their center distance, a contact would be identified and established; otherwise, no contact exists between the two particles. And the orientation of each detected contact can be determined through the coordination of the two particle centers.

The contact force magnitude is quantified through the fringe patterns in the polarized image. Mahabadi and Jang (2017) experimentally established a linear relationship between the contact force magnitude and the effective fringe distance, which was defined as the distance measured from the contact point to the last fringe pattern (lowest red color pixel value) before the particle center. The magnitude of all the contact forces are extracted from the fringe patterns in the polarized image. The force chain network is then reconstructed with all the required quantitative information.

RESULTS AND DISCUSSIONS

Tip resistive force. Figure 3 shows the evolution of the tip resistive force during the test. The tip resistive force increases rapidly at both "foot" penetration stages (A and E, in Figure 3), but decreases at the "shell" expansion stages (C and D, in Figure 3). The increment in tip resistive force for both "foot" penetration stages are both around 70 N, and the total reduction due to expansion is about 42 N, which is equivalent to 44% in reduction. Moreover, tip resistive force during the rest time are not stable and tends to rebound back to a relatively higher value.

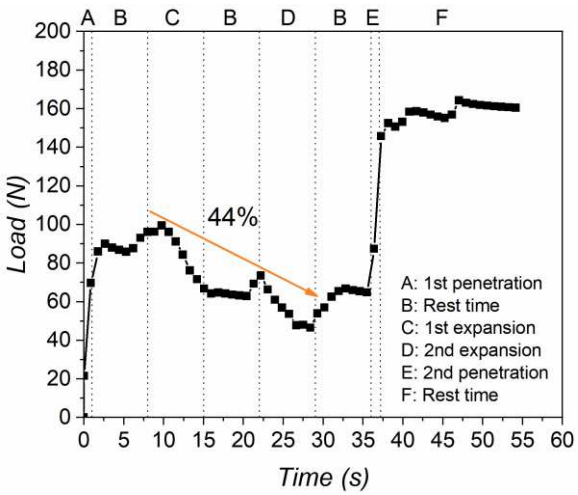

Figure 3. Tip resistive force evolution during the test.

Force chain network. To illustrate the penetrator kinematics and the corresponding force chain network during the test, images are taken at four different moments in the test, and the force chain network for each moment is reconstructed and presented in Figure 4.

Some interesting features of force chain distribution can be identified. Overall, the strong force chains are mainly perpendicular to the contact boundaries ("foot", "shell" and cell boundary). The "shell" expansion mainly introduces horizontal strong force chains (Figure 4b, 4c), while the strong force chains around the "foot" caused by penetrations are inclined and perpendicular to the "foot" surfaces (Figure 4a); right below the "foot", the strong force chains are nearly vertical; away from the "foot", the force chains are also affected by the boundaries of the "shell" and cell. When both "shell" expansion and "foot" penetration co-exist in the sample, the force chain patterns become complex (see Figure 4b,4c and 4d).

A clear force chain evolution pattern is identified from Figure 4. As shown in the original polarized images(figure on the left of each section in Figure 4): 1. the initial "foot" penetration induces strong force chain network around and below the "foot", with very sparse strong force chains on both sides of the "shell" (Figure 4a); 2. with the proceeding of "shell" expansion, new strong force chains appear along the expanding "shell", whereas the strong force chains around the "foot" formed in the 1st penetration stage become sparser (Figure 4b and 4c); 3. the 2nd "foot" penetration further compacts the particles and forms intensive and radially distributed strong force chains around the "foot"; whereas the strong force chains around the "shell", which are formed during the "shell" expansion, become sparser (see Figure 4d). The reconstructed force chain network captures the key features of the force chain evolution pattern, as presented in figures on the right-hand side of each section in Figure 4. The results provide an intuitive explanation of the macroscale tip resistive force evolution as indicated by the load cell readings.

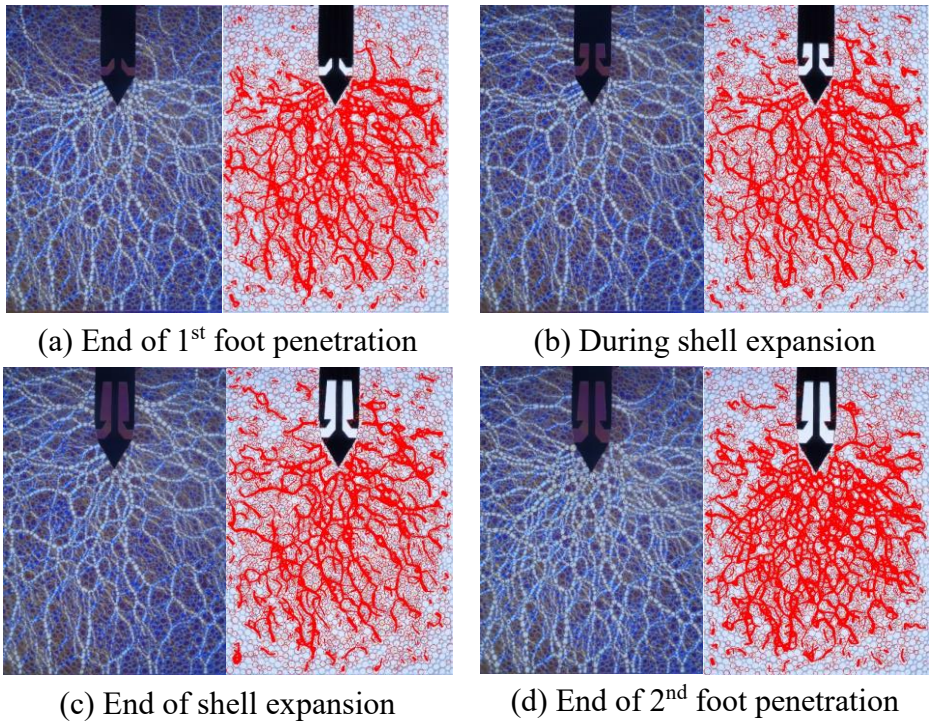

(a) End of 1st foot penetration (b) During shell expansion

(c) End of shell expansion (d) End of 2nd foot penetration

Figure 4. Force chain evolution during the test. For each section, figure on the left shows the penetrator kinematic and the associated fringe patterns appearing on the photoelastic particles; figure on the right represents the reconstructed force chain network based on the distributed fringe patterns across the sample.

Load transfer. Another way to quantify the force chain evolution and load transfer is to compare the forces by conducting pixel subtracting operations to images taken at different moments. The light intensity (or pixel values) indicates the local force magnitude applied on the photoelastic disks. Orientation of the fringe pattern (or light path) on each disk represents the direction of the force. By subtracting the red channel intensity values of two different polarized images, force development zones and force relaxation zones are obtained.

Figure 5 presents the difference between the moments at the end of 1st "foot" penetration and at the end of "shell" expansion (Figure 5a, b) and that between the moments at the end of "shell" expansion and at the end of 2nd "foot" penetration (Figure 5c, 5d). Figure 5a shows the force development zone by the end of "shell" expansion. In general, significant compressive forces appear around the expanded "shell" and extend towards the external boundary, which are consistent with the strong force chains indicated in Figure 4c. The concentrated high contact forces also demonstrate the contribution of the "shell" expansion to the formation of a penetration anchor by increasing the lateral confinement applied on the expanded "shell". It is also interesting to find that the compressive forces close to the upper boundary transmits in a more horizontal direction, while the compressive forces close to the level of foot-and-shell interface transmits laterally but inclines downward to external boundary. Several small force chains are also developed around and

below the triangular "foot", with an intensity decreasing with increasing depth. The appearance of the small force chains around the "foot" is mainly due to the local particle rearrangement.

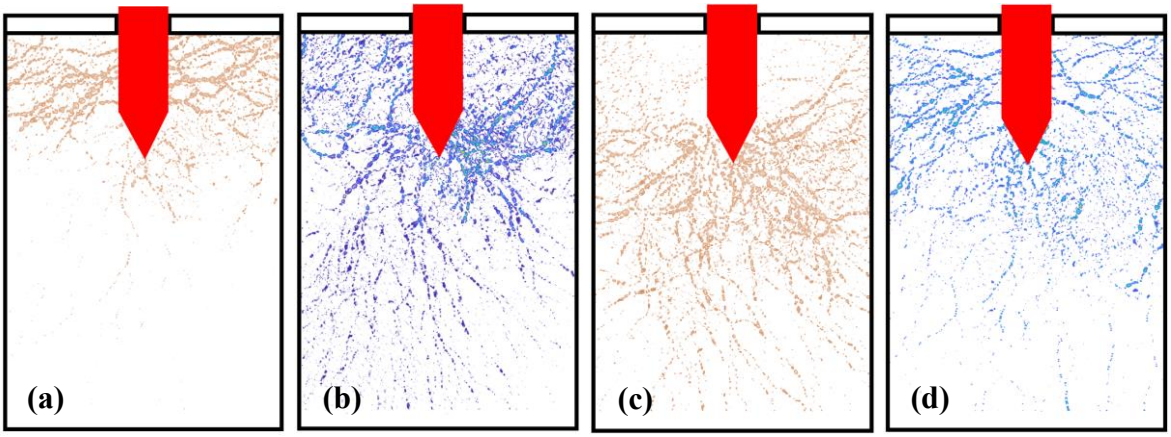

Figure 5. Interplay between shell opening and foot penetration. The melon color zone in (a) and (c) indicate the force development created by the shell opening and the foot penetration, respectively; the blue color zone in (b) and (d) indicate the force relaxation created by the shell opening and the foot penetration, respectively.

In addition to the force development along the "shell", expansion of the "shell" also causes significant force relaxation inside the granular sample, which mainly concentrates around the "foot", and become attenuated towards the outer boundary (Figure 5b). It is interesting to see that force reduction also happens above the "foot" and these forces are more inclined to the vertical direction. Figure 5a and 5b together indicates rotation of the principal stresses along the shell.

Similarly, difference between the end of 2nd "foot" penetration and the end of "shell" expansion is obtained to study the impact of "foot" penetration, as shown in Figure 5c and 5d. As expected, the load transfer pattern reverses, comparing to the observation in Figure 5a and 5c. The introduction of 2nd "foot" penetration not only re-establishes the concentrated strong force chain network below the cone, but also relaxes the forces along the "shell". This observation indicates that the "foot" penetration weakens the penetration anchorage by reducing the forces applied around the expanded "shell"; the penetration is limited to small advancements to take advantage of the high anchorage formed during "shell" expansion.

Discussions. The visualization and extraction of particle contact forces with the use of photoelasticity and image processing provides us an intuitive view on how the force chains evolve corresponding to the complex penetration kinematics. Without "shell" expansion, advancement of the "foot" compacts the particles around and below the "foot", causing radially distributed strong force chains around the "foot" (see Figure 4a). The geometrical distribution of the strong force chains is similar to the displacement field around the cone or pile tip during cone penetration/pile installation (Arshad et al. 2014; Salgado 2012; Toiya et al. 2007; White and Bolton 2004; Zhang and Wang 2015): particles right below the cone tip experience vertical displacement; particles

around the cone experience a displacement transition from vertical to horizontal direction; and for other regions particles tend to being displaced horizontally. Granular material below the advancing "foot" sustains earth pressure and experiences compressive force; the deeper the soil, the higher the effective stress and therefore the harder to fail the soil by compression-induced shearing. In such a case, penetrating to a deeper position requires a higher thrust to fail the granular material and to create space for the advancing "foot".

However, by expanding the "shell", the load transfers from the "foot" to the "shell". The expanding "shell" compressed the photoelastic particles right on both sides and induced a high compressive zone; whereas particles around the level of "foot"-and-"shell" interface are driven laterally under the combined effect of interparticle friction and rolling resistance. Both force development and force relaxation exist around the level of "foot"-and-"shell" interface (see Figure 5). Consequently, the loading condition of the particles around the interface level is more similar to that in a typical direct shear test. Particulate structure continuously evolves with strong force chains breaking around the "foot" and re-establishing around the "shell", causing a decrease of the macroscale tip resistive force.

The 2nd "foot" penetration re-load the particles around and below the "foot", resulting in the concentration of strong force chains. Meanwhile, particles along the newly developed force chains are compressed, indicating a compressive straining behavior (see Figure 5c); whereas particles close to the expanded "shell" locate within an obvious force relaxation zone (see Figure 5d), indicating a extensile straining behavior. The general distribution of compression and extension zones is consistent with our previous numerical findings (Huang and Tao 2018b). With the tensile deformation around the expanded "shell", the penetration anchorage formed by the "shell" expansion becomes weakened.

The interplay between the shell-opening and foot-penetration is a complex soil-structure interaction problem, which depends on various parameters, such as the shape of shell and foot, shell expansion ratio (defined as the ratio of shell size increment divided by the original shell size), shell expanding rate, foot penetration rate, soil conditions. The current study only considers the interplay under a specific set of conditions: rectangular shell and triangular foot, a shell expansion ratio of 12%, a shell expanding rate of ~1mm/s and a foot penetration rate of ~1cm/s, and a specific particulate sample. The degree of force development and relaxation during "shell" expansion and "foot" penetration may vary under different combinations of all the parameters mentioned above and deserves a further investigation.

A limitation of the current setup is that the force chain network close to the image boundary and around the shell cannot be completely reconstructed. This is caused by the sample illumination and camera view angles. The camera view angle is perpendicular to the acrylic chamber center (area around the foot), but become increasingly deviated for areas away from the chamber center, especially at the chamber boundary. As a result, shadows of the particles away from the cell center appear in the images, which casts noise in the particle extraction and the associated contact detection, as indicated in Figure 4. Also, current design of the penetrator only allows small shell expansion ratios. In the future work, multiple cameras and better lighting condition will be used to

avoid particle shadows; filtering technologies, such as the median and Gaussian filtering methods adopted by (Nguyen and Indraratna 2019; Zhao et al. 2015), will be introduced to remove the noisy particle shadows and to enhance image quality for the subsequent image processing; and new penetrators will be designed to accommodate larger expansion ratios. With complete extraction of the particles and contact forces, more quantitative analysis (e.g., fabric tensor) can be conducted to shed light on the fundamental mechanism of complex penetration phenomena like self-burrowing behavior of living organisms and future self-burrowing robots.

CONCLUSION

This study utilizes a combined technique of photoelasticity and image processing to visualize the interplay between "shell" opening and "foot" penetration of a model razor clam, emphasizing on the analysis of force chain evolution. Results indicate that the force chain network induced by "foot" penetration qualitatively matches the displacement field observed in a typical cone penetration test or pile installation test (Arshad et al. 2014; White and Bolton 2004). More importantly, the mutual effects between the "shell" expansion and "foot" penetration is confirmed: "shell" expansion compresses the surrounding particles and induce strong lateral force chains around the "shell", contributing to the formation of a penetration anchor by increasing the lateral confinement; at the same time, it causes the weakening of the strong force chains around and below the "foot" and thus reducing the penetration resistance; on the other hand, the "foot" penetration after the "shell" expansion re-establishes the strong force chains around the foot but induces a force relaxation zone around the expanded "shell", leading to the weakening of the penetration anchorage. Such interplay is important when studying the burrowing mechanics of living organisms and designing bioinspired self-burrowing robots: expansion induced reduction of penetration resistance may be a strategy to increase the burrowing efficiency; but penetration induced relaxation of the anchorage may compromise the burrowing effectiveness.

REFERENCES

Abdalla, A., Hettiaratchi, D., and Reece, A. (1969). "The mechanics of root growth in granular media." *Journal of Agricultural Engineering Research*, 14(3), 236-248.

Arroyo, M., Butlanska, J., Gens, A., Calvetti, F., and Jamiolkowski, M. (2011). "Cone penetration tests in a virtual calibration chamber." *Geotechnique*, 61(6), 525-531.

Arshad, M., Tehrani, F., Prezzi, M., and Salgado, R. (2014). "Experimental study of cone penetration in silica sand using digital image correlation." *Geotechnique*, 64(7), 551-569.

Bolton, M. D., Gui, M.-W., Garnier, J., Corte, J. F., Bagge, G., Laue, J., and Renzi, R. (1999). "Centrifuge cone penetration tests in sand." *Géotechnique*, 49(4), 543-552.

Budhu, M. (2008). *SOIL MECHANICS AND FOUNDATIONS, (With CD)*, John Wiley & Sons.

Daniels, K. E., Kollmer, J. E., and Puckett, J. G. (2017). "Photoelastic force measurements in granular materials." *Review of Scientific Instruments*, 88(5), 051808.

Das, B. M. (2013). *Advanced soil mechanics*, Crc Press.

Dorgan, K. M. (2015). "The biomechanics of burrowing and boring." *J Exp Biol*, 218(Pt 2), 176-183.

Holland, A., and Dean, J. (1977). "The biology of the stout razor clamTagelus plebeius: I. Animal-sediment relationships, feeding mechanism, and community biology." *Chesapeake Science*, 18(1), 58-66.

Huang, S., and Tao, J. (2018a). "Modeling of the Burrowing Mechanism by Razor Clam: Role of Penetration Kinematics." *IFCEE 2018: Advances in Geomaterial Modeling and Site Characterization*, 295.

Huang, S., and Tao, J. (2018b). "The interplay between shell opening and foot penetration of a model razor clam: Insights from DEM simulation." *B2G Atlanta 2018 Bio-mediated and Bio-inspired Geotechnics*.

Jung, S., Winter, A. G., and Hosoi, A. (2011). "Dynamics of digging in wet soil." *International Journal of Non-Linear Mechanics*, 46(4), 602-606.

Mahabadi, N., and Jang, J. (2017). "The impact of fluid flow on force chains in granular media." *Applied Physics Letters*, 110(4), 041907.

Maladen, R. D., Ding, Y., Umbanhowar, P. B., and Goldman, D. I. (2011). "Undulatory swimming in sand: experimental and simulation studies of a robotic sandfish." *The International Journal of Robotics Research*, 30(7), 793-805.

Nguyen, T. T., and Indraratna, B. (2019). "Micro-CT Scanning to Examine Soil Clogging Behavior of Natural Fiber Drains." *Journal of Geotechnical and Geoenvironmental Engineering*, 145(9), 04019037.

Salgado, R. (2012). "The mechanics of cone penetration: Contributions from experimental and theoretical studies." *Geotechnical and Geophysical Characterization*, 4, 131-153.

Toiya, M., Hettinga, J., and Losert, W. (2007). "3D Imaging of particle motion during penetrometer testing." *Granular Matter*, 9(5), 323-329.

Trueman, E. (1967). "The dynamics of burrowing in Ensis (Bivalvia)." *Proceedings of the Royal Society of London B: Biological Sciences*, 166(1005), 459-476.

White, D., and Bolton, M. (2004). "Displacement and strain paths during plane-strain model pile installation in sand." *Géotechnique*, 54(6), 375-397.

Winter, A., Deits, R., Dorsch, D., Slocum, A., and Hosoi, A. (2014). "Razor clam to RoboClam: burrowing drag reduction mechanisms and their robotic adaptation." *Bioinspiration & biomimetics*, 9(3), 036009.

Winter, A. G., Deits, R. L. H., and Hosoi, A. E. (2012). "Localized fluidization burrowing mechanics of Ensis directus." *Journal of Experimental Biology*, 215(12), 2072-2080.

Zhang, Z., and Wang, Y.-H. (2015). "Three-dimensional DEM simulations of monotonic jacking in sand." *Granular Matter*, 17(3), 359-376.

Zhao, B., Wang, J., Coop, M., Viggiani, G., and Jiang, M. (2015). "An investigation of single sand particle fracture using X-ray micro-tomography." *Géotechnique*, 65(8), 625-641.